FABRICATION AND TESTING OF SILICON INTEGRATED
NANOFLUIDIC CHANNELS FOR NEUROCHEMICAL TRANSPORT

BY

ARI ESTERS

THESIS

Submitted in partial fulfillment of the requirements
for the degree of Master of Science in Electrical and Computer Engineering
in the Graduate College of the
University of Illinois at Urbana-Champaign, 2018

Urbana, Illinois

Adviser:

Professor Yurii Vlasov

ABSTRACT

Several neurosensing techniques have been developed to study neurological activity in mammalian brains, though none of these methods fully satisfy the requirements for high-resolution neurochemical sensing. Therefore, to fulfill this need, we have developed a process to build a monolithic neurochemical sampling probe in which the size and spatial resolution can be directly controlled. Moreover, we have developed test benches to characterize the fluidic and chemical transport properties of the device, which is directly related to the temporal resolution. However, upon testing, we discovered that fluid flow is not possible through either of the two devices fabricated thus far, which is in disagreement with our flow simulation results. For the next step, we will build test structures to measure the performance of the nanofluidic channels without probe integration to determine the root cause of this issue. Upon resolving this issue, we will be able to measure the temporal resolution of various integrated probe designs to optimize the performance of our nanofluidic device.

To my brother, parents, and grandparents, for their love and support.

ACKNOWLEDGMENTS

TABLE OF CONTENTS

CHAPTER 1

INTRODUCTION

Correlating neural activity with pathophysiology and behavior in non-anesthetized mammals is critical to decoding the neuronal circuitry of mammalian brains and developing better treatments for neurological disorders. High-resolution neural sensing devices are needed to achieve this feat. In particular, ideal biosensors should allow for robust detection of electrical or chemical signals localized to a specific region of the brain (high spatial resolution) in real time (high temporal resolution) and with sufficient sensitivity (surpassing limit-of-detection), all while causing minimal brain damage during use.

Numerous biosensing methods have been developed, including fluorescence imaging-based methods for real-time molecular tracking, fast scan cyclic voltammetry, electrical probes, and chemical sampling probes [1-11]. However, none of these methods currently meet all the requirements of an ideal biosensor. Namely, in addition to high spatiotemporal resolution, recording the concentration of multiple chemicals simultaneously is vital since animal behavior is driven by several neurotransmitters and neuromodulators [6, 12]. Fluorescence methods and fast-scan cyclic voltammetry are typically limited to a single neurochemical species at a time, offering very limited information on brain physiology [6, 7]. Moreover, electrical probes that can only sense electrical impulses omit the useful physiological information encoded in the neurochemical dynamics of the brain. On the other hand, the use of chemical sampling probes allows for multiplexed chemical sensing since the sampled contents can be directly analyzed using high-sensitivity tools such as mass spectrometry [12-16]. However, chemical analysis must be implemented ex vivo to determine the chemical contents of the samples. Because of the amount of tubing and fluidic transport required to connect sampling probes with ex vivo analysis methods, push-pull and microdialysis tend to suffer from poor temporal resolution (several seconds to minutes) due to

1

Taylor dispersion [12, 15, 17-22]. Past work has been able to negate Taylor dispersion in chemical probes to some degree using flow segmentation [11, 15, 20-22], though dispersion effects persist in the flow prior to segmentation and careful design must be considered to prevent droplet merging. Additionally, the need for integrated fluidic channels can limit miniaturization of the probe, leading to rather bulky probe cross sections (>200 µm diameter) that can cause significant brain damage upon implantation [3, 15, 23].

Current sensing methods fail to meet the specifications needed for neurological research. Thus, we plan to develop a neurochemical sensing platform combining silicon nanofluidics and silicon probe fabrication to simultaneously achieve high spatial resolution, high temporal resolution, robust chemical sensing, and low invasiveness. Fabricating the probe and fluidic components entirely in silicon allows us to achieve high spatial resolution and a small probe cross section using standard microfabrication processes, and the temporal resolution can be improved by careful channel design and fluidic engineering techniques. In particular, we aim to build silicon fluidic channels that can sample chemicals in a small area less than 100 µm^2, achieve subsecond temporal resolution, and operate at a depth of less than 10 µm such that the channels can be integrated on an ultrathin silicon probe. Chapter 2 describes the design and fabrication of the silicon microchannels, including fluidic parameters considered in their design. Chapter 3 describes the setup and implementation of a plug-and-play experimental setup for measuring the fluidic and chemical transport properties of various channel designs, and Chapter 4 discusses the outcome of the first experiments using this setup.

CHAPTER 2

CHANNEL FABRICATION AND DESIGN

2.1   Fabrication

Figure 2.1 shows the mask layout for a silicon probe. The thin red lines represent the silicon microchannels, the white lines form the outline of the silicon probe, and the green circles are the plumbing holes for inserting glass capillaries. The channels are fabricated first, followed by additional patterning and deep etching steps to form the probe outline, etch down to the desired probe thickness, and release the probe from the wafer. Then, the probe is packaged using custom parts and fitted with glass capillaries that serve as the junction between the silicon channels and plastic tubing.
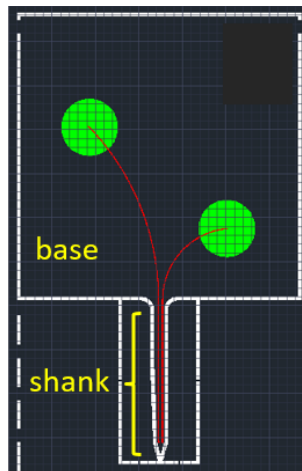

Figure 2.1: Multi-layer mask layout for silicon probe in AutoCAD.

The silicon probe, which is to be implanted into the brain of an animal, should be as thin as possible to minimize brain damage. The main limit to minimizing the thickness of the probe is the depth of the silicon channels needed for fluidic transport. Therefore, the channel structures in this work

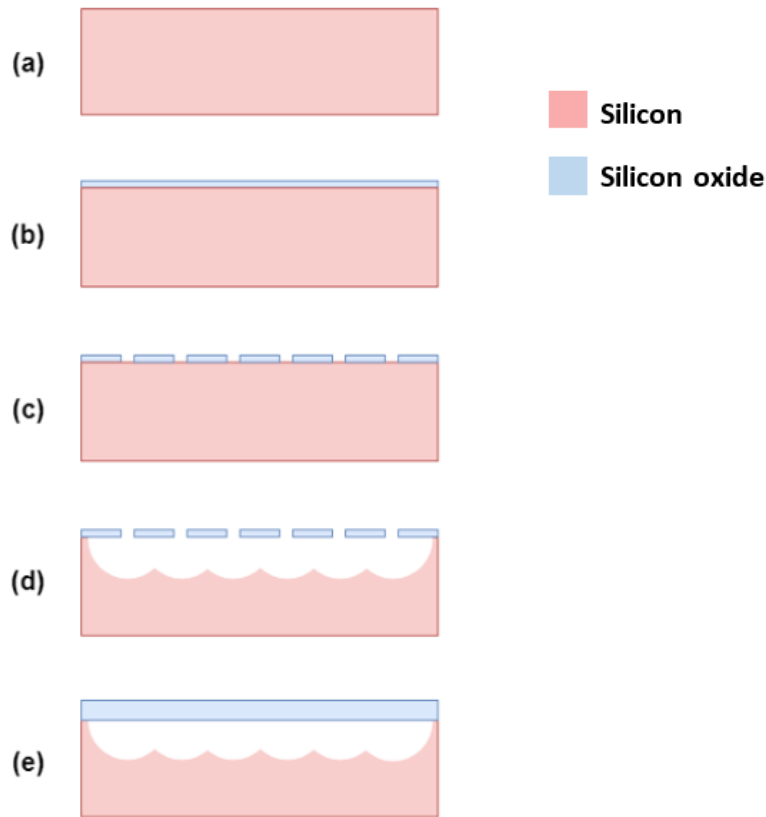are largely confined to a maximum width of 50 µm and a maximum depth of 10 µm.

Figure 2.2: Fabrication workflow for bulk silicon channels.

2.1.1 Thermal Oxidation

These channels are constructed using standard semiconductor processing tools. Starting with a silicon substrate (Figure 2.2a), a thin film of silicon oxide (SiO_2) is grown by dry thermal oxidation (Figure 2.2b). First, the sample is cleaned by piranha solution for 2 minutes. The sample is then placed in a glass wafer tray and loaded into a thermal furnace preset to 400 degrees C. The furnace is set to 1150 degrees C while nitrogen gas is continuously fed into the furnace to provide an inert environment. Once the furnace reaches 1150 degrees C (after about 40 minutes), the nitrogen valve is closed and oxygen is fed into the tube at a rate of 5 L/min to begin the oxidation process. After one hour, the oxygen valve is closed and the nitrogen valve is re-opened. The furnace is set back to 400 degrees C and allowed to

cool down (takes 2-3 hours). Once the furnace has cooled to 400 degrees C, the sample is unloaded and allowed to cool to room temperature. The thermal oxide thickness of the sample is typically in the range of 150-170 nm after one hour of dry oxidation. The exact thickness can be found using an ellipsometer.

2.1.2 Photolithography and ICP RIE Etch

Next, a pattern of 1.5-µm holes spaced 4 µm apart is etched into the oxide layer (Figure 2.2c). This is achieved by contact lithography followed by plasma etching. First, an adhesion promoter (HMDS) is spin-coated onto the sample using a two-step spin recipe: (1) 500 rpm setpoint with 5000 rpm/s ramp for 2 seconds, followed by (2) 5000 rpm setpoint with 5000 rpm/s ramp for 20 seconds. Then, AZ1512 photoresist is spin-coated onto the sample using the same spin recipe. If available, a shield can be placed around the wafer before spin-coating to improve the uniformity of the photoresist film. After spin-coating, the sample is placed on a 110 degree C hot plate for 1 minute and allowed to cool to room temperature for 1 minute. Using the EVG 620 mask aligner, the sample and photomask are brought into contact using a vacuum, and the sample is exposed through the patterned mask at a dosage of 55 mJ/cm^2 with an i-line source (365 nm light). Then, the sample is placed in a manually stirred AZ developer solution for 2 minutes, rinsed with deionized (DI) water, and dried with nitrogen.

The aforementioned procedure describes a process that has been calibrated to approach our target feature size of 1.5 µm. In actuality, the feature size will vary from sample to sample or between different locations on the same sample. Namely, the resulting feature size on the substrate depends on the uniformity of the initial photoresist film and the exposure dosage. If the photoresist film is not uniform after spin-coating, then substrate and photomask will not be in perfect contact during exposure, leading to larger feature sizes or features with shallow side angles (compare Figures 2.3 and 2.4). If the side angle of the photoresist feature is shallow, then the side angle of the subsequent etching step will be shallow as well, and the final feature size would not be well-controlled. Most of the variability from die to die or from wafer to wafer arises from non-uniformities in the photoresist film. Addi-

tionally, the feature size also varies with exposure dosage. Even while using the same photomask, the exposure dosage can be used to tune the width of the developed features. Greater exposure dosages lead to larger feature sizes, whereas lower dosages lead to smaller feature sizes but with greater variability (Figure 2.5). However, if the dosage is too low, then the feature will not develop in the photoresist at all. Thus, careful calibration of the photolithography process is needed to obtain the desired feature size.
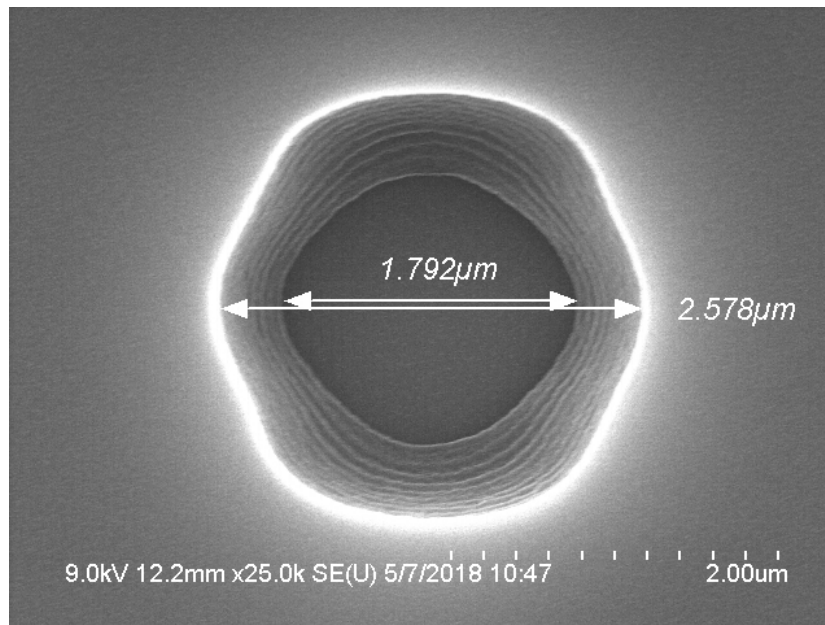

Figure 2.3: SEM image of feature in photoresist. Shallow side angles can form if the contact between the substrate and photomask are insufficient. Note the large difference between the inner and outer widths.
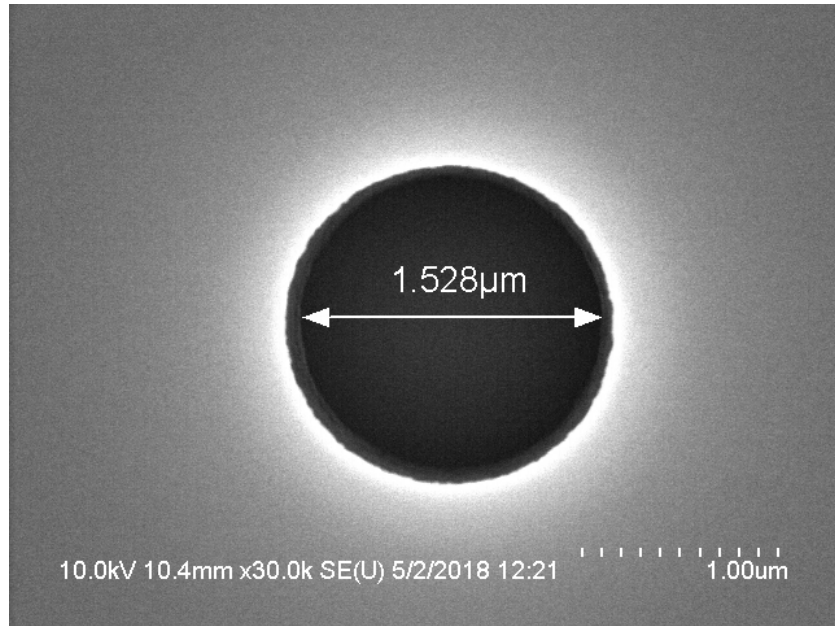
Figure 2.4: SEM image of feature in photoresist. Steep side angles in the photoresist features are indicative of good contact between the substrate and photomask.
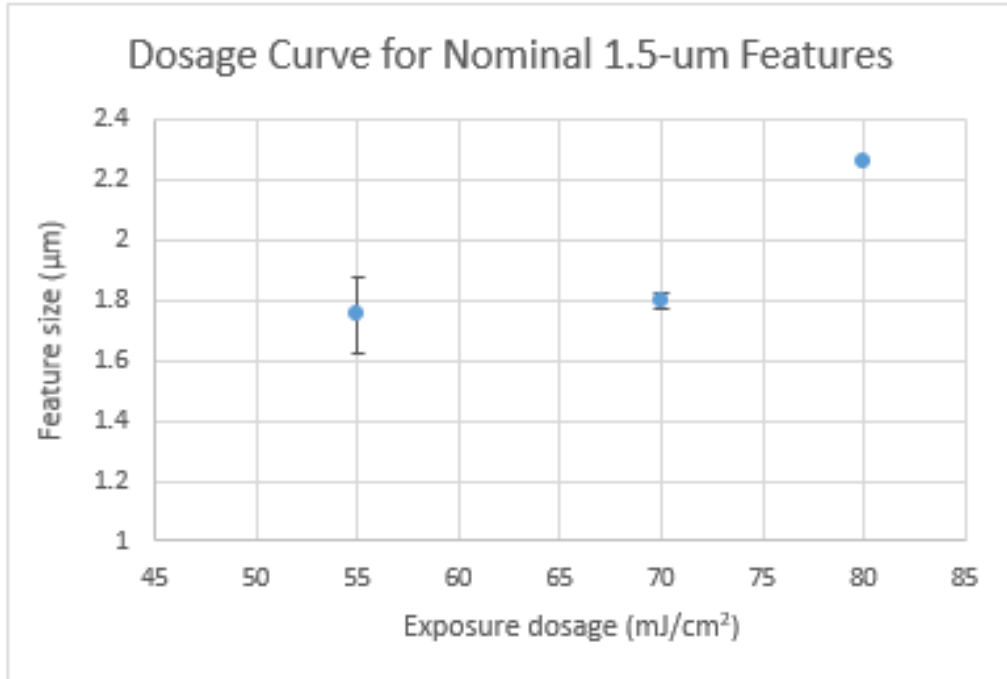
Figure 2.5: Feature widths obtained from 1.5-µm features in the photomask exposed at different dosages. Each data point is the mean of three samples (excluding the 80 mJ/cm^2 datapoint, which is the result of one sample). Black bars indicate the standard deviation.

After exposure and development, the sample is placed in an ICP RIE chamber to etch the exposed oxide. The precise etching time depends on the oxide film thickness and the etching parameters. For the Oxford Freon ICP RIE tool in the Micro and Nanotechnology Lab (MNTL) at the University of Illinois, the standard etch recipe for SiO$_2$ has an etch rate of about 200 nm/min for dry thermal oxide, which is suitable for our film thickness. Finally, the photoresist film is removed by submerging the sample in AZ400T photoresist stripper at 90 degrees C for 20 min, followed by a 5 min sonication in isopropanol and a DI water to completely clean the surface.

2.1.3   Channel Formation by XeF$_2$ Etch

After the photoresist film is removed, channels are formed in silicon by XeF$_2$ etching (Figure 2.2d). The etching is performed in a Xactix XeF$_2$ system under 3 Torr pressure of XeF$_2$ vapor. The etch rate of silicon under XeF$_2$ strongly depends on the amount of exposed silicon in the sample. Thus, for

every new channel design, the sample should be exposed to XeF_2 for a short time (i.e., 60 seconds or less) and imaged with scanning electron microscopy (SEM) to determine the etch rate. After the etch rate has been established, the XeF_2 etch time can be calculated based on the desired channel dimensions.

2.1.4 Channel Sealing by PECVD

Once the silicon channels have been etched, the channels are sealed by chemical vapor deposition (CVD) of SiO_2 (Figure 2.2e). As SiO_2 is deposited onto the substrate, some SiO_2 molecules will deposit on the edges of the holes suspended above the channels, reducing their diameter. We have created a simple model predicting the degree to which each feature size decreases during CVD. In particular, the relationship between the initial diameter of an opening d_i and its final diameter after deposition d_f is given by

$$d_f = d_i - 2St_{dep} \tag{2.1}$$

where t_{dep} is the thickness of SiO_2 deposited onto the substrate, and S is the side growth parameter. We have defined this side growth parameter as the ratio of the horizontal growth on the edge of the openings to the total thickness of SiO_2 deposited, and this ratio physically must be less than unity. Moreover, to seal our channels with CVD, the openings must be closed by the end of the process ($d_f = 0$). In other words, the criterion for channel sealing by CVD is given by

$$t_{dep} = \frac{d_i}{2S} \ . \tag{2.2}$$

We hypothesized that the value for S depends on both the tool and conditions (e.g., temperature, pressure, etc.) used for deposition. Therefore, we experimentally measured this parameter in different CVD tools and recipes by measuring the diameter of suspended holes before and after deposition of 1 µm of SiO_2. Among the tools considered were three plasma-enhanced chemical vapor deposition (PECVD) tools in MNTL and one low-pressure chemical vapor deposition (LPCVD) tool in the Birck Nanotechnology Center at Purdue University. The side growth and deposition rate for each tool are reported in Figure 2.6. The deposition rate for the LPCVD tool is not

9

known since this tool is operated by an external vendor.

As suggested by Equation 2.2, a higher side growth parameter is desired such that less deposition would be required to seal our channels. However, our experiments suggest that the side growth parameter does not vary greatly between these CVD tools. Thus, we ultimately decided to use the Trion PECVD tool for our fabrication since this tool is capable of significantly faster deposition rates. Based on Equation 2.2, sealing 1.5-µm openings using the Trion PECVD ($S = 0.40$) requires about 1.9 µm of deposited material. However, this deposition thickness describes the critical point at which the openings have just been closed. To strengthen the oxide film above our channels, we deposit a total of 3-4 µm of SiO_2 with the Trion PECVD tool. Figure 2.7 shows an SEM cross section of four parallel channels fabricated using this procedure.

Deposition Tool	Side growth parameter (%)	Deposition Rate (nm/min)
MNTL Plasmalab PECVD	0.50 (50%)	33
MNTL Trion PECVD (fast dep recipe)	0.40 (40%)	118.6
MNTL Trion PECVD (slow dep recipe)	0.49 (49%)	36.2
Purdue LPCVD	0.39 (39%)	-

Figure 2.6: Side growth parameter and deposition rates for different CVD tools.
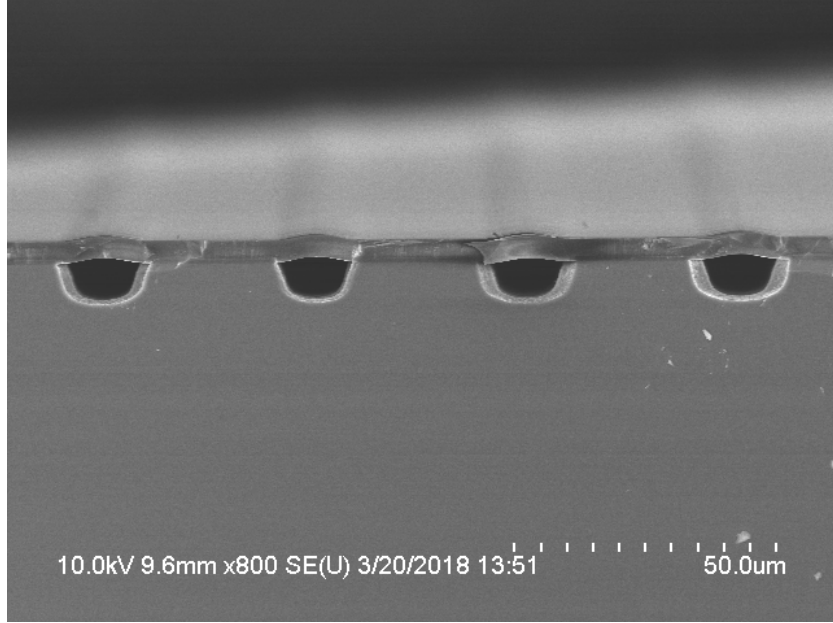
Figure 2.7: SEM cross section of four parallel channels viewed edge-on. The channels extend in the direction away from the detector.

2.1.5   Channel Structure Characterization by FIB

To determine whether the openings are completely closed, a precise cross section is obtained using a focused ion beam (FIB). The depressions in the top surface of the channel in Figure 2.8 indicate the previous locations of the openings. However, an overhead SEM image does not provide enough resolution to conclude whether the opening is completely closed. Therefore, a FIB cross section is etched through one of these depressions to obtain a high-resolution image of the integrity of the oxide film (Figure 2.9). From the cross section, we can see that the oxide film directly under the depression is intact, indicating that the opening has been completely sealed by SiO_2 deposition.
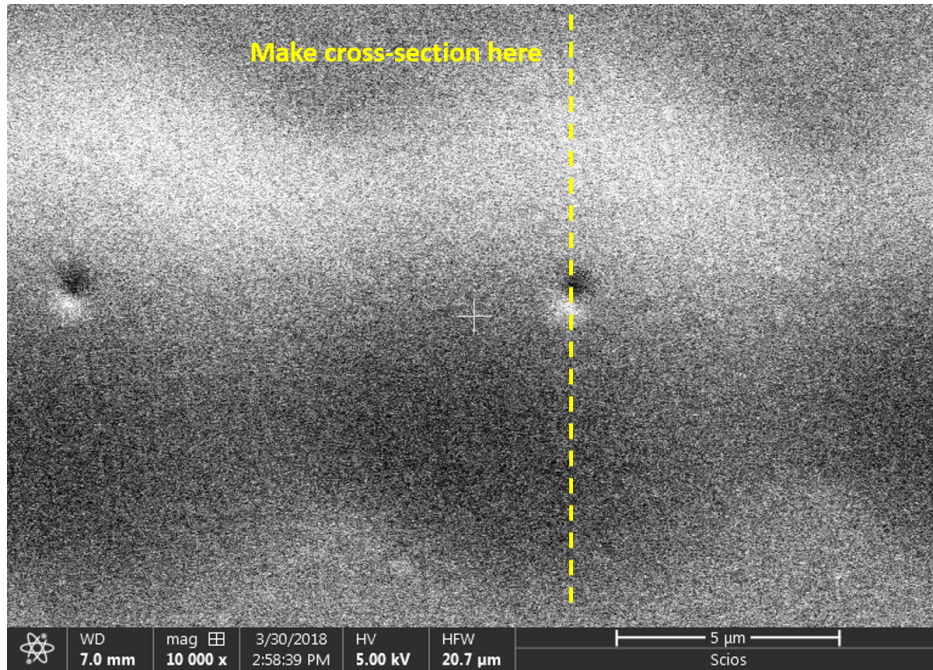
Figure 2.8: SEM overhead image with dashed line indicating where cross section will be performed (white plus sign marks center of image).
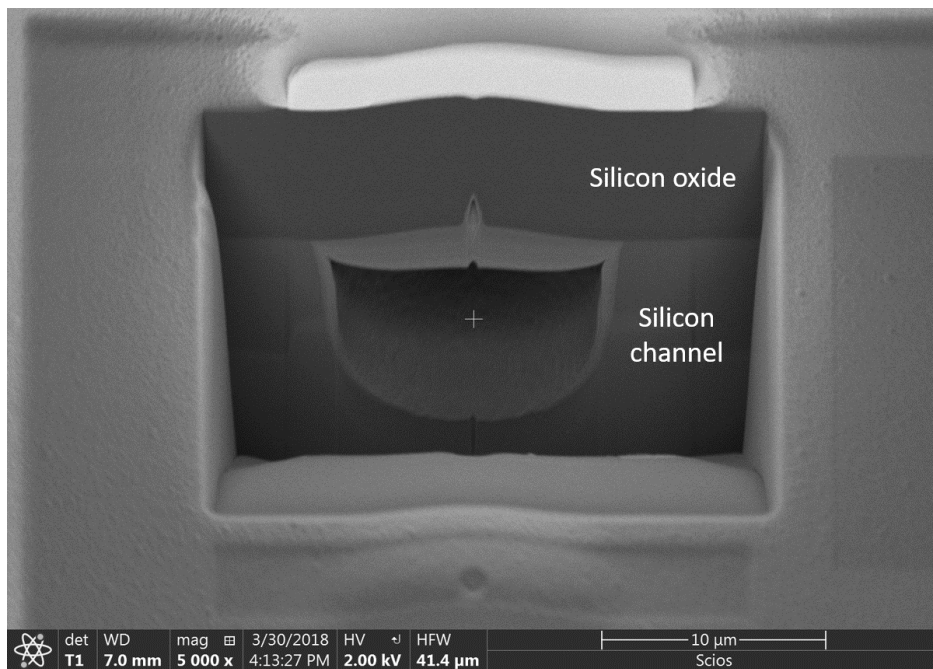

Figure 2.9: FIB cross section of silicon channel showing integrity of oxide film (white plus sign marks center of image).

2.1.6   Microchannel Configurations

In the process described in Figure 2.2, the length of the microchannels is strictly controlled by the pattern length in Figure 2.2c, and the channel radius is controlled by the etch time in Figure 2.2d. Therefore, microchannels of various dimensions can be fabricated in a straightforward manner. The precise channel dimensions needed to meet our target spatiotemporal resolution is determined by the fluidic and chemical transport properties, discussed in more detail in Sections 2.2 and 2.3.

The channel geometry and pattern near the tip of the probe shank is varied to yield multiple fluidic configurations. Chemical probe technology is generally divided into two categories, push-pull and microdialysis. We have designed silicon nanofluidic channels in both push-pull (Figure 2.10) and microdialysis (Figure 2.11) configurations. Several other variations of push-pull and microdialysis structures have been designed and fabricated as well; the images shown are but two examples.
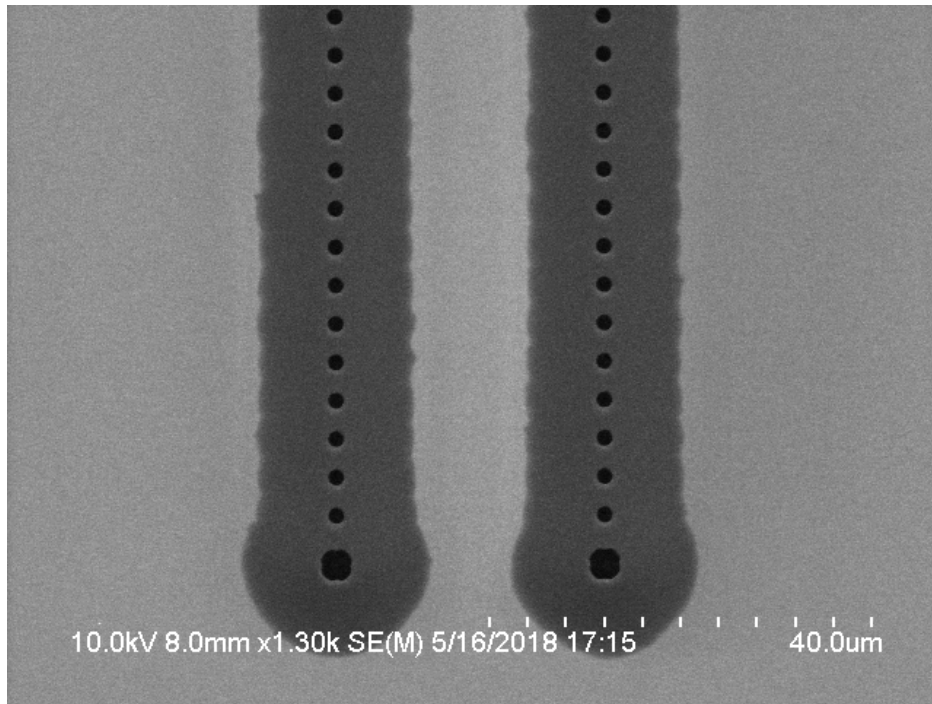

Figure 2.10: SEM overhead image of silicon push-pull channels before final deposition step.
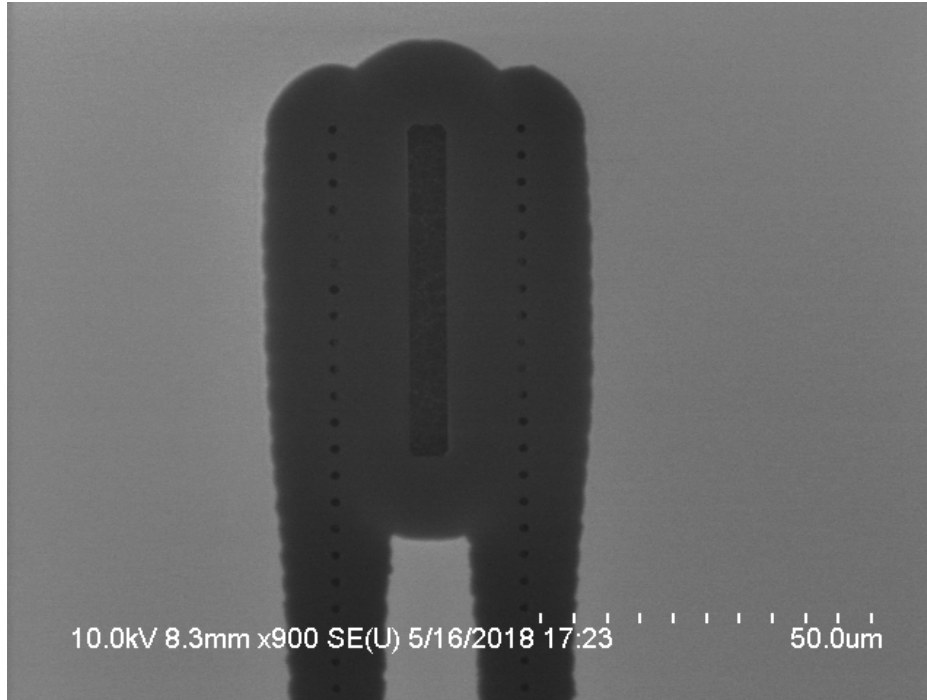
Figure 2.11: SEM overhead image of silicon microdialysis channels before final deposition step.

These channel images were taken before the final deposition step. Note that the buried channel is plainly visible in the overhead SEM images since the overlying oxide thickness is very thin at this stage of the process. In the final deposition step, the deposition thickness is adjusted such that the smaller holes shown in the images are closed during deposition while the larger holes remain open, resulting in sealed channels with small openings for chemical exchange. In a push-pull configuration, the two fluidic channels are completely separate, as shown in Figure 2.10, and are thus driven by different pumps. When operated *in vivo*, one fluidic channel is used to retrieve fluid from the brain extracellular matrix, and the other channel is used to pump artificial cerebrospinal fluid (aCSF) into the brain to maintain constant volume. In a microdialysis configuration, the two channels meet near the tip of the probe to form a closed fluidic circuit, and a semipermeable membrane allows selective chemical exchange between the channel and the surrounding brain volume. Figure 2.11 shows the structural foundation for this type of configuration, where the large open rectangle designates the area onto which the membrane would be transferred. Both push-pull and microdialysis both enable direct sampling of the brain microenvironment and are

14

therefore robust methods for neurochemical sensing. In each structure, the area over which chemical exchange occurs is directly controlled at the design level, allowing for localized chemical sampling with high spatial resolution. Hence, we have devised a simple process for fabricating silicon channels that can lead to the development of ultrathin silicon probes with high spatial resolution.

2.2 Modeling Fluidic Transport

As shown in the previous section, nanofluidic channels of various dimensions can be easily fabricated in bulk silicon using well-known, controllable semiconductor processes. However, further considerations are required to determine the channel dimensions and flow parameters required to meet our target spatiotemporal resolution.

The extremely small cross section of these channels essentially guarantees any fluid flow will be in the laminar flow regime. However, the cross section and corrugations within the channel will affect the overall hydrodynamic resistance. Therefore, a laminar flow model is constructed in COMSOL to determine the pressures required to achieve certain flow rates in these channels. The geometric model shown consists of a volume generated by conjoining 8-µm-radius hemispheres whose centers are spaced 4 µm apart to emulate our channel design (Figure 2.12).
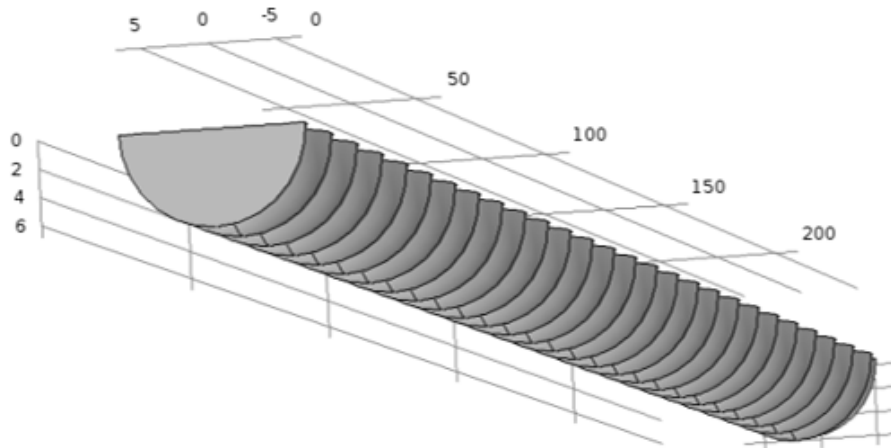

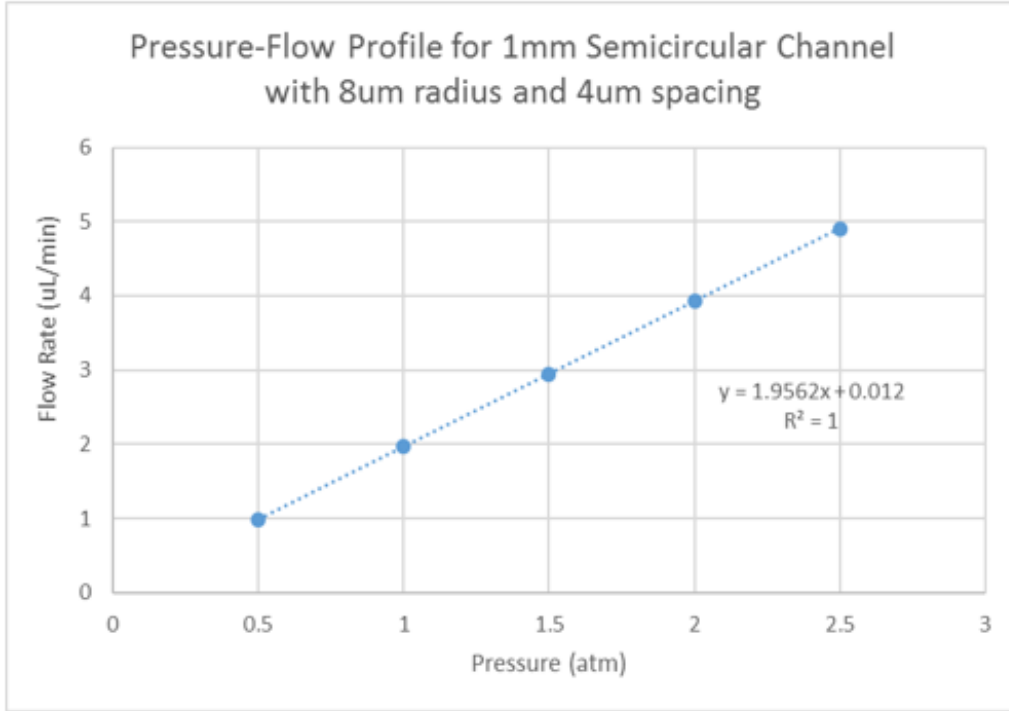Figure 2.12: COMSOL geometric model for silicon channel with corrugations.

Figure 2.13: Laminar flow simulation results for silicon microchannel.

Pressured-induced flow through this geometric model shows a linear dependence between flow rate and pressure, with a 1-mm long channel generating about 2 µL/min flow per atm of applied pressure (Figure 2.13). Additionally, under laminar flow conditions, the pressure needed (ΔP) to induce a particular flow rate (Q) increases linearly with channel length (L), so the total required pressure is determined by:

$$\Delta P \, [\text{atm}] = \frac{Q \, [\text{µL/min}] \; L \, [\text{mm}]}{1.96} \tag{2.3}$$

The fluidic channels used in our design range from about 2 to 5 mm in length. Thus, using Equation 2.3, the pressure range needed to generate between 0.05 and 5 µL/min flow rates in our longest channels (5 mm) is between 0.13 and 13 atm. The model suggests that it is possible to induce a large range of nanofluidic and microfluidic flow rates in our silicon channels using pressure differentials that can easily be generated by commercial pumps.

16

2.3 Modeling Chemical Transport: Taylor Dispersion

Taylor dispersion severely limits the temporal resolution observed in fluidics-based biosensors. For example, when using push-pull or microdialysis probes, neurochemical responses in the brain of the subject will manifest as spikes in neurotransmitter concentration, which can be sampled and transported by fluidic flow through the probe. However, as shown in laminar flow simulations (Figure 2.14), Taylor dispersion can significantly increase the spread of a sharp concentration signal over relatively short times and distances. If the signal broadening is significant enough, adjacent neurochemical signals traveling in the fluidic channel will begin to overlap, causing consecutive neurochemical events to be indistinguishable.

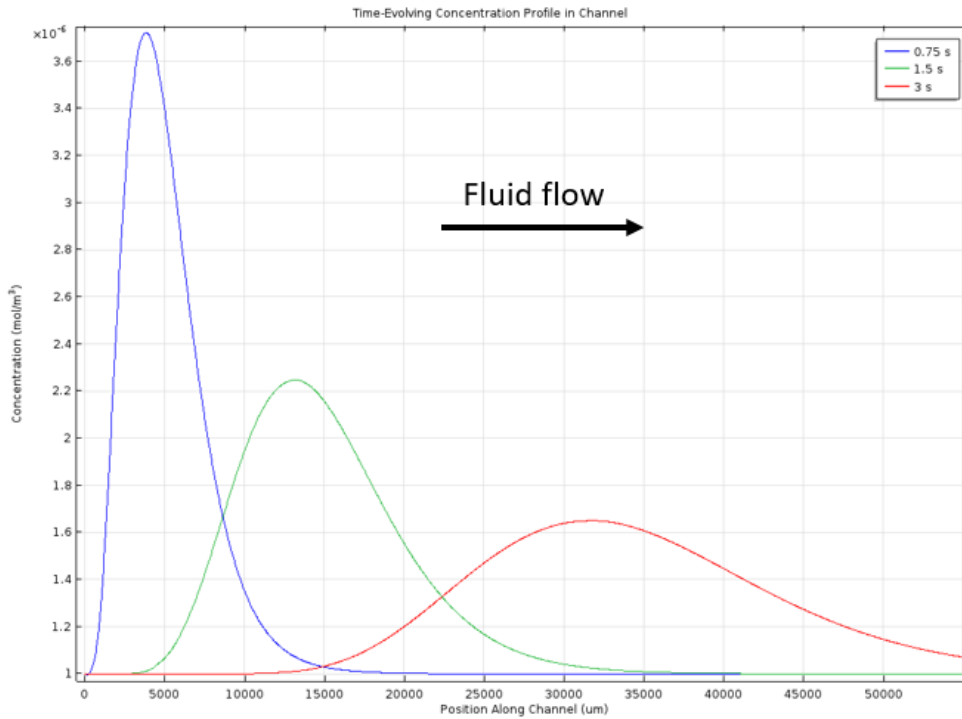Figure 2.14: Simulation of sharp chemical signal deformed by 1 µL/min fluid flow in a nanofluidic channel.

Taylor dispersion is observed whenever there is a non-uniform concentration in a flowing solution [24]. Under laminar flow conditions, the governing equation for Taylor dispersion is given by:

$$\frac{\partial C_{avg}}{\partial t} = k \frac{\partial^2 C_{avg}}{\partial x_1^2} \tag{2.4}$$

17

where C_{avg} is the concentration averaged in the lateral direction, k is the dispersion coefficient, t is time, x_1 is the position of the center of the concentration distribution. The equation takes the same form as the time-dependent diffusion equation, except in this case x_1 is the position of a moving reference frame whose velocity is determined by the flow rate of the liquid. In actuality, Taylor dispersion is not caused by mere diffusion, but by two concurrent physical phenomena: the longitudinal distortion of the concentration profile in the direction of flow, and the lateral diffusion of the concentration profile which leads to mostly uniform concentration in the lateral direction. Thus, the magnitude of Taylor dispersion depends not only on the diffusion coefficient of the analyte, but also on flow parameters such as the flow rate and cross section of the fluidic channel. This is demonstrated in the analytical solution for the dispersion coefficient in a cylindrical channel [24]:

$$k = \frac{a^2 u_0^2}{192D} = \frac{a^2 u_{avg}^2}{48D} \tag{2.5}$$

where a is the channel radius, u_0 is the max fluid velocity, u_{avg} is the average fluid velocity, and D is the diffusion coefficient of the solute. Additionally, the channel length plays a major role in the amount of Taylor dispersion observed. In fact, longer flow paths result in more severe Taylor dispersion since the chemical signal spends more time in a flowing solution.

Prior work has used fluid segmentation to encapsulate chemical signals into droplets to prevent further Taylor dispersion and loss of temporal resolution [11, 15, 20-22]. However, Taylor dispersion still affects the chemical signals during transport to the droplet generation device, which is typically placed several centimeters away from the sampling location. Thus, our goal is to quantify and minimize Taylor dispersion effects in our probe and fluidic system wherever possible by tuning controllable parameters such as the flow rate and channel dimensions. Of course, incorporating droplet generation into the fluidic circuit could greatly improve the temporal resolution of the device, but that is beyond the scope of this work, which focuses on proof of concept and characterization of single-phase flow devices.
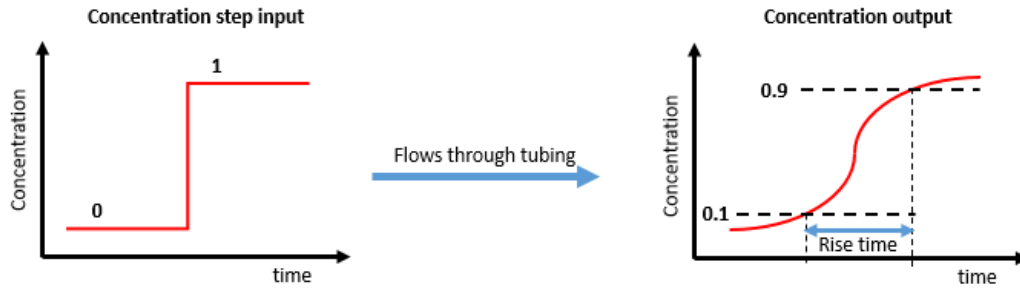
Figure 2.15: Graphic demonstrating how rise time is calculated.

One quantitative indicator of the strength of Taylor dispersion within a fluidic path is rise time [17, 19-22]. Due to Taylor dispersion, an instantaneous concentration step applied to the input of a flowing channel will be distorted in the direction of flow at the output. The rise time is calculated by measuring the time it takes for the outlet concentration to rise from 10% to 90% of the concentration step (Figure 2.15). Stronger Taylor dispersion results in greater distortion of this concentration step and hence longer rise times. Therefore, minimizing the rise time is equivalent to reducing Taylor dispersion and improving the temporal resolution of the flow system.

CHAPTER 3

EXPERIMENTS

We have fabricated and packaged the first iterations of silicon probes for single-phase flow using the silicon nanofluidic channels described in this work. To test these devices, we propose a setup that enables us to characterize their fluidic and chemical transport properties (Figure 3.1). In this setup, up to two syringe pumps will control fluid flow through the device. The beaker contains a continuously stirred solution with a known concentration of some physiologically relevant chemical, such as dopamine or serotonin, dissolved in artificial cerebrospinal fluid (aCSF). One syringe pump draws fluid from the solution through the probe and analysis chip. The analysis chip continuously measures the concentration of the dissolved analyte as the fluid passes through the chip. The concentration input to the device and analysis chip can be controlled by the concentration in the beaker. For example, a concentration step can be applied by adding a small amount of highly concentrated solution to the stirred beaker. Then, the rise time from this step change can be observed from the time-varying concentration response measured in the analysis chip. The rise time will indicate the severity of Taylor dispersion in the flow path from the probe tip to the analysis chip, with the microchannel design on the probe being the only variable between successive experiments.
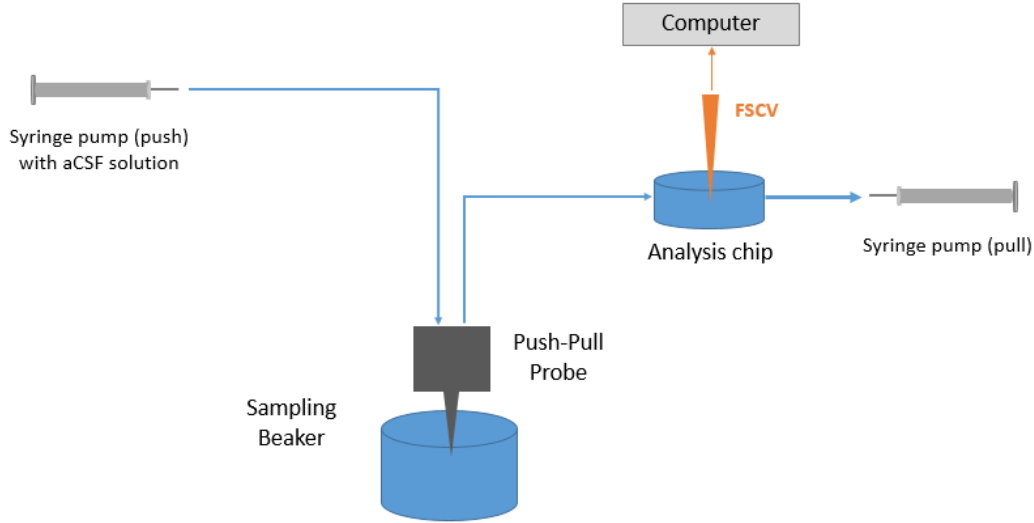
Figure 3.1: Illustration of test bench for characterizing silicon probes.

The ultimate goal of these experiments is to identify silicon channel designs that result in optimal temporal resolution for our chemical probe. At present, this test bench has been separated into two modules being developed in parallel: fluidic transport testing and chemical transport testing. These modules are described in detail in the following sections.

3.1   Fluidic Transport Module

The first module constitutes the left side of Figure 3.1 and comprises a syringe pump connected by plastic tubing to the capillaries of the packaged probe, which is either held in air or in solution. An overhead microscope is used to visually detect signs of fluid flow or leakage on the probe, as shown in Figure 3.2. This setup can be used to pump fluid from the syringe pump into the probe, or operated in reverse to pull fluid from the solution through the probe. Either operating mode can be used to validate whether the packaged device is capable of the fluid flow predicted in COMSOL simulations. The experiment can be repeated with different flow rates set on the syringe pump to determine the operating flow range of the device.
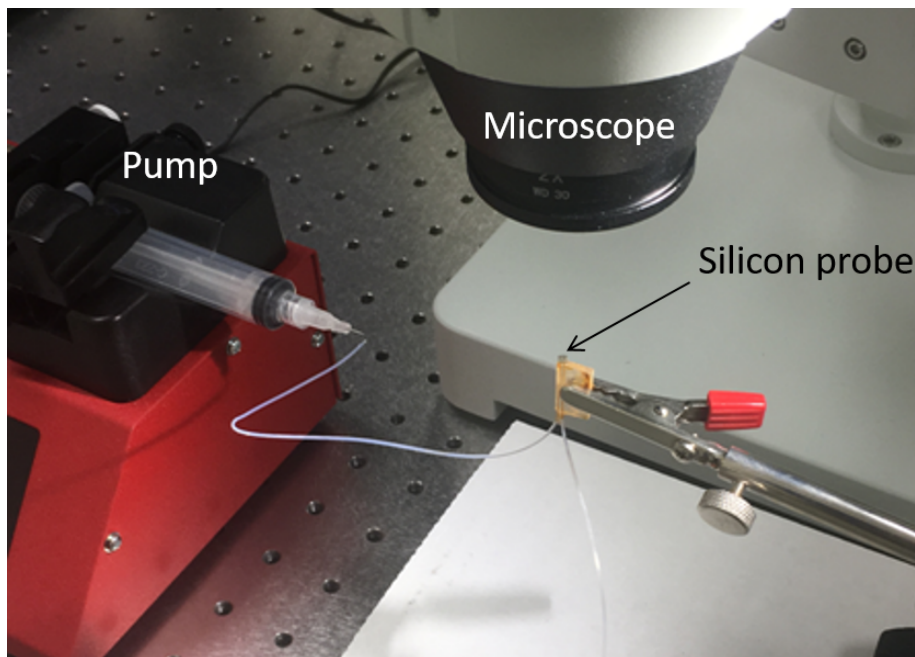
Figure 3.2: Setup for testing fluid flow through silicon probes.

With this setup, we tested two silicon probes using two different tests. In the first test, a syringe is filled with DI water, and the packaged probe is held in the air by clamps while DI water is pumped from the syringe to the probe using a syringe pump. A positive result for fluid flow in this test would be the observation of water appearing along the shank of the silicon probe. In the second test, the syringe is initially empty, and the packaged probe is held in DI water while the syringe pump is operated in reverse to pull fluid through the probe and toward the syringe. A positive result for fluid flow in the second test would be the observation of water moving in the capillaries and tubing connecting the probe to the pump.

3.2   Chemical Transport Module

The second module constitutes the right side of Figure 3.1, comprising a syringe pump drawing fluid from a continuously stirred solution, through the probe, and through an analysis chip that continuously measures the analyte concentration in the solution. After applying a sharp change in concentration in the solution, the change in concentration will be distorted by Taylor dispersion, leading to an extended rise time measured at the analysis chip.

This rise time serves as a quantification of the degree of Taylor dispersion occurring between the solution and the analysis chip. Hence, if testing multiple probe designs, probes with lower rise times have less Taylor dispersion, corresponding to better temporal resolution.

In this work, no probes are tested with the chemical transport module. The experiments involved in this module correspond to the development of the analysis chip, which is crucial to the proposed experiment setup. To test the efficacy of the analysis chip, we use a syringe pump to continuously pump a solution of dopamine dissolved in phosphate-buffered saline (PBS) from a stirred beaker and through the analysis chip. The analysis chip uses fast-scan cyclic voltammetry (FSCV) to continuously measure dopamine concentration. Then, the dopamine concentration in the stirred beaker is suddenly increased by 40 µM (from 10 µM to 50 µM) by the addition of a highly concentrated dopamine solution. The flow rate is set to 10 µL/min on the syringe pump and is unchanged throughout the course of this experiment. The experiment is allowed to run for 60 minutes.

3.2.1 FSCV Operation

FSCV is used to measure the analyte concentration in this setup (Figure 3.3). As mentioned previously, FSCV is ill-suited for the simultaneous monitoring of multiple analytes, limiting its *in vivo* applications. However, because of its high spatial and temporal resolution, FSCV is a superior analytical tool for measuring transient concentrations of a single chemical. Also, FSCV has high chemical sensitivity and can detect very small changes in concentration. We tested the sensitivity of FSCV by attempting to measure dopamine signals in various PBS solutions with known concentrations of dopamine. We found that FSCV can reliably detect changes in dopamine concentration as small as 0.4 nM. Therefore, FSCV is a perfect candidate for in vitro experiments that require high-resolution chemical sensing. We have decided to use this tool to measure and understand how our nanofluidic transport system fares with fast changes in concentration, which is directly relevant to the *in vivo* practicality of our design.
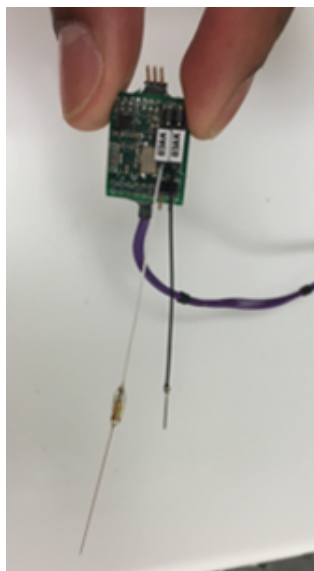
Figure 3.3: Image of FSCV hardware showing printed circuit board connected to two electrodes.

FSCV operates by applying a time-varying bias voltage between two electrodes. Under any bias voltage, the resulting current measured between the electrodes depends on the chemical and ionic content of the solution. However, by applying certain voltage waveforms, the oxidation and reduction of certain chemicals can be detected. An example of the input and output for FSCV is shown in Figure 3.4. The triangle waveform is specifically used to detect dopamine. Then, by subtracting the background current due to the PBS buffer, it is possible to detect the current signatures of dopamine arising from dopamine redox reactions (Figure 3.5). The strength of these redox peaks is related to the concentration of dopamine in the buffer. The background current is obtained by applying the triangle waveform to PBS with no dopamine added.
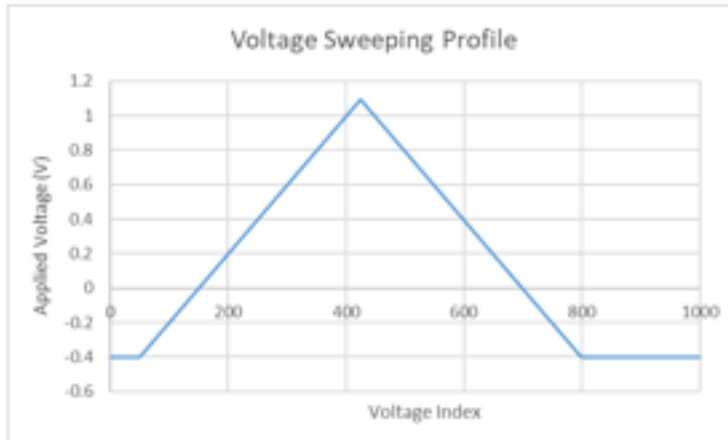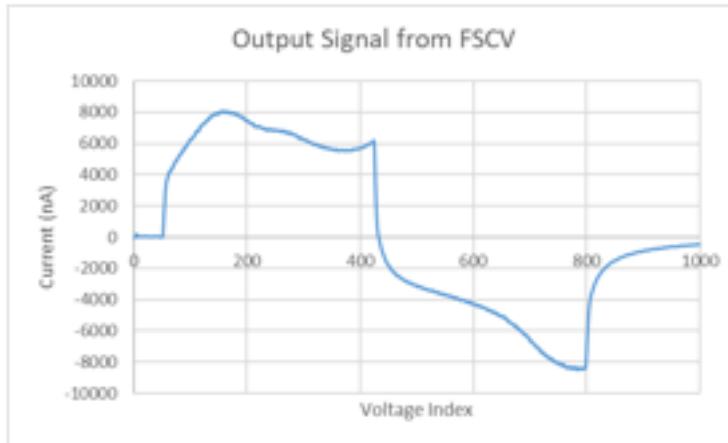
Figure 3.4: FSCV applies triangular voltage waveform to solution (top) and measures the resulting current (bottom). The x-axis represents time progression of a single sweep (duration of 100 milliseconds).
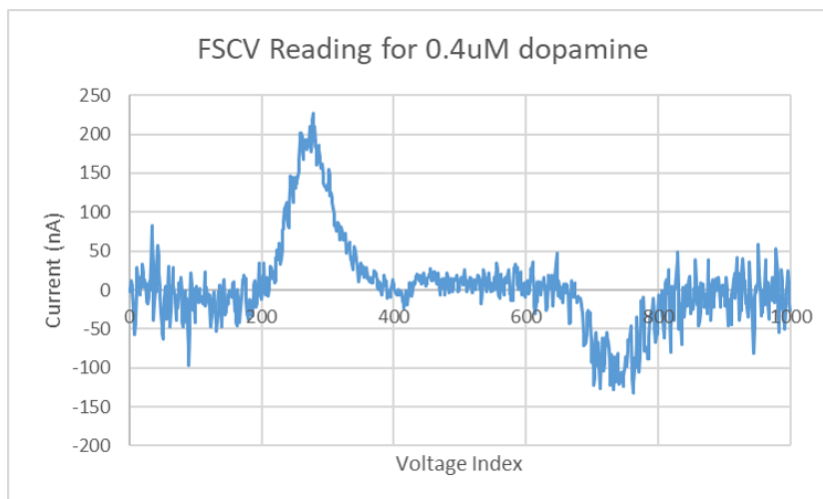
Figure 3.5: Background is subtracted from FSCV output to reveal current signature of dopamine.

The commercial FSCV system used in this work comes with hardware designed to apply voltage waveforms and read the response current as well as acquisition software to configure voltage sweeping parameters for the hardware. This system can sweep through the triangle waveform in as short as 100 milliseconds. The software can collect data from one or multiple voltage sweeps and save each collection of sweeps into separate files, referred to here as scans. In the acquisition software, we set the duration of each scan to be 20 seconds. In other words, each saved file contains 200 triangular voltage sweeps, with each sweep providing potential data on dopamine concentration.

3.2.2   Analysis Chip Fabrication

To enable continuous FSCV measurements in a flowing solution, we have fabricated a PDMS chip with channels whose dimensions are 2 mm by 2 mm by 3 cm. The FSCV electrodes are inserted into the channel through the top of the PDMS chip (Figure 3.6). To fabricate the PDMS chip, the PDMS base and curing agent are mixed thoroughly in a 10:1 ratio. The PDMS is poured into a petri dish containing the mold for our channels. This mold could be a 3D-printed part or silicon wafer with pre-processed structures, depending on the desired dimensions and shape for the PDMS channels. The petri dish is placed in a degassing chamber for 1 hour or until almost all air bubbles are removed. Next, the petri dish is placed in an 80 degree C oven for at

least 2 hours to cure the PDMS. Once the petri dish is removed from the oven, the PDMS is carefully peeled from the petri dish and mold. If the PDMS contains several channel structures, then a sharp blade is used to cut out a single channel. Then, using a straight 23-gauge syringe needle, four puncture holes are made in the channel: one puncture near each end of the channel, and two punctures close to the center of the channel. These punctures represent the locations of the fluidic inlet and outlet (at channel edges) and the FSCV electrodes (near channel center).
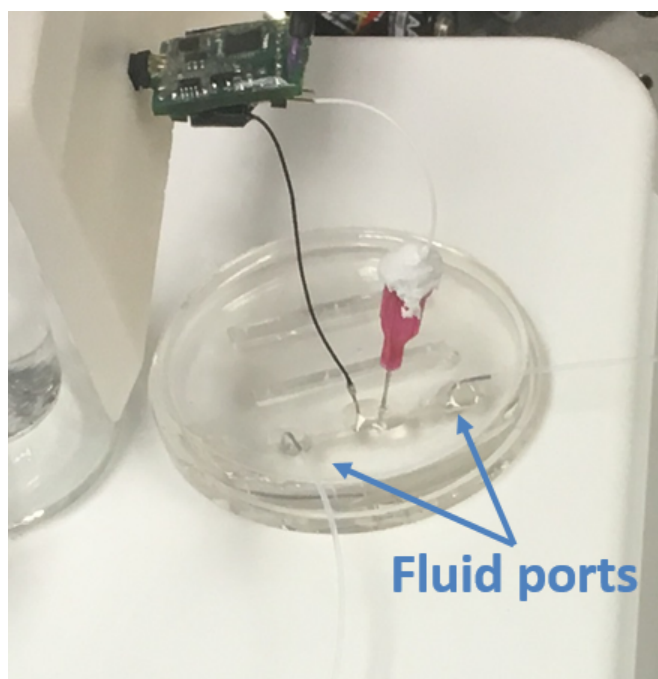
Figure 3.6: Analysis chip for measuring chemical transport with FSCV electrodes inserted from the top.

To remove any debris from puncturing, the PDMS is sonicated in an isopropanol solution for 15 minutes. The PDMS is dried with a nitrogen gun and left to air-dry for 1 hour. As a final cleaning step, a strip of tape can be used to remove any remaining dust or particulates. Then, PDMS must be bonded to a flat surface (silicon wafer or another PDMS layer) in order to enclose the channels. To accomplish this, the surfaces that will be bonded are placed face-up in a Diener oxygen plasma system and exposed to oxygen plasma for 2 minutes. Once the surfaces are removed from the chamber, the PDMS is quickly placed onto the flat surface such that the plasma-exposed surfaces make contact, forming the enclosure that will act as the PDMS

channel. There is no need to apply any additional force, as the surfaces have been activated by oxygen plasma and bonding occurs naturally. To further encourage bonding, the PDMS channel is placed onto a hot plate set to 175 degrees C for 15 minutes. Then, the PDMS channel is set aside for 24 hours at room temperature to ensure that the interior of the channel passivates before further fabrication.

The last step in PDMS chip fabrication is the insertion of the fluid ports and FSCV electrodes. For the fluid ports, the metal part of two 90-degree-bent 27-gauge syringe needles are removed using scissors or a sharp blade. These metal connectors are inserted into the puncture holes near the ends of each channel, and plastic tubing with an inner diameter of 320 µm is connected to the metal to form the fluid ports for the PDMS channels. Next, the ground FSCV electrode (thicker electrode) is directly inserted into the PDMS channel through one of the puncture holes near the center of the channel. A straight 23-gauge syringe needle is inserted into the remaining puncture hole, and the positive electrode (thinner electrode) is carefully threaded through the needle. At this point, it is important to ensure that all four inserted objects intersect the channel volume, which we accomplish with the use of a handheld microscope. Finally, to seal the PDMS punctures, epoxy resin is applied around all insertion points in PDMS, and epoxy putty is placed at the top of the syringe needle holding the positive FSCV electrode. The complete PDMS chip is set aside for 24 hours while the epoxy fully cures.

3.3   Automated Analysis in MATLAB

We have written a MATLAB script to handle the large amount of data generated by this experiment. This script plots the measured redox current over time and can convert this data to concentration values. A high-level description of the script is illustrated in Figure 3.7.
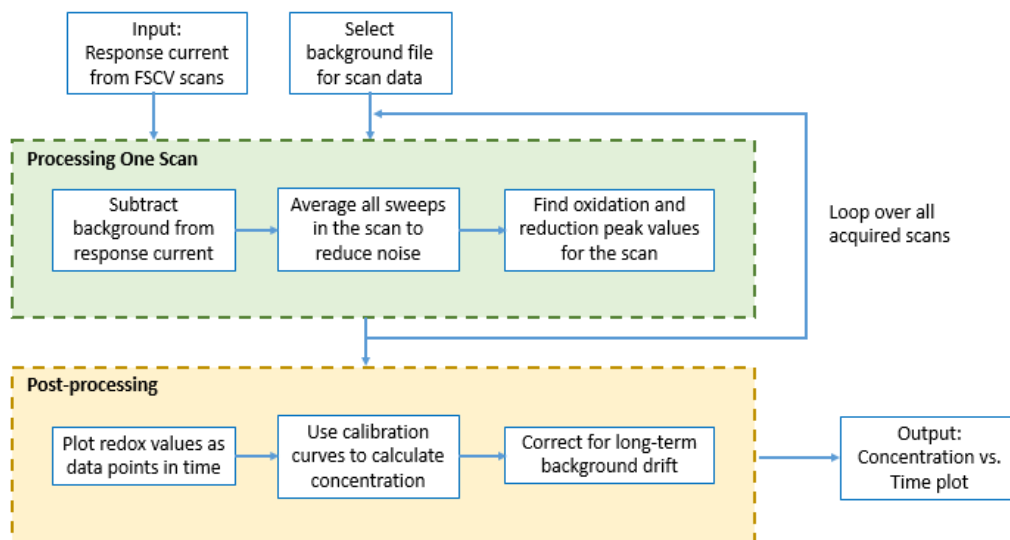
Figure 3.7: Block flow diagram for MATLAB analysis script.

The MATLAB script accepts experiment files from the FSCV acquisition software as an input. Each experiment file contains the measured current from 200 voltage sweeps. After selecting a background file, the script begins to process the acquired scans one at a time. First, the background current is subtracted from the scan. Next, the current from each sweep in the scan is averaged to reduce noise levels, and the average redox peak values are stored. These steps are repeated for each scan in the experiment folder. Once all the scans have been processed, the redox values are converted to concentrations using the pre- or post-calibration data and plotted on a time axis based on the scan duration and order of acquisition. The output of the script is a concentration vs. time plot spanning the length of the experiment.

CHAPTER 4

RESULTS AND DISCUSSION

4.1 Testing Fluidic Transport

The COMSOL model presented in Section 2.2 predicts that we should be able to access a wide range of flow rates using our nanofluidic channels. However, with our current setup, we were not able to achieve any type of fluid flow through the packaged silicon probes. One possible reason is that the flow resistance through our channels is significantly larger than expected. The hydrodynamic resistance of nanofluidic and microfluidic channels can be higher than predicted due to the small width of the perfusion openings (less than 3 µm) at the ends of the channel. Another possible cause for this negative result is clogging from the adhesive. The packaging procedure of the silicon probe involves connecting the capillaries to the probe using epoxy resin. We have previously observed that during this packaging procedure, the epoxy can seep into the plumbing hole and obstruct the flow path. It is not yet clear whether one or both of these causes are impeding fluid flow in our probe. To eliminate possible causes, our next mask version will include low-resistance channels (e.g., channels with short length) directly connecting two capillary ports. Furthermore, these test channels can be operated in the silicon wafer and will not require probe fabrication and release. If the negative result in our original experiment is due to hydrodynamic resistance, then fluid flow through the low-resistance test channels should be possible using the same experiment setup. If flow is still impeded in the test channels, then the issue is likely due to a blockage introduced during the insertion of the capillaries. These low-resistance test structures will allow us to quickly determine the cause of flow obstruction without the added complexity of probe integration.

4.2 Testing Chemical Transport

In the chemical transport experiment, we were able to obtain data from the analysis chip (Figure 4.1) that resembles the concentration step applied in the beaker.
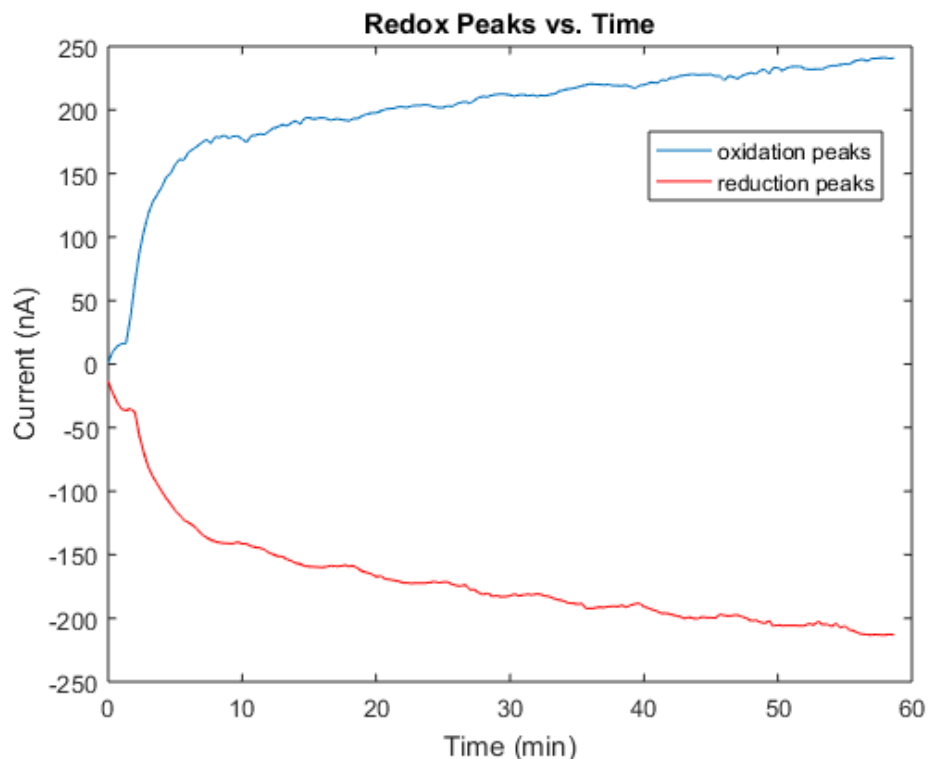

Figure 4.1: Plot showing oxidation/reduction current over time. Current drifts steadily at longer times.

Using MATLAB, the oxidation and reduction current for dopamine is plotted over time. There was no calibration done for this pair of electrodes, so the corresponding dopamine concentrations are not given. Nevertheless, based on past calibrations, we expect that the oxidation and reduction current to be approximately linear to the concentration for relatively small concentration changes. Thus, the shape of the concentration plot will closely resemble the redox plot, and transient parameters such as rise time should be nearly identical between the two. After about 15 minutes, the concentration at the analysis chip reaches steady-state, marked by the point where the slope of the redox curve decreases significantly and remains constant. However, even after this point, the redox current appears to change due to a drift in back-

ground current that commonly manifests in FSCV experiments [1]. The plot can be corrected for long-term background drift by fitting a linear curve to the steady-state regime and subtracting this curve from the experiment data (Figure 4.2).
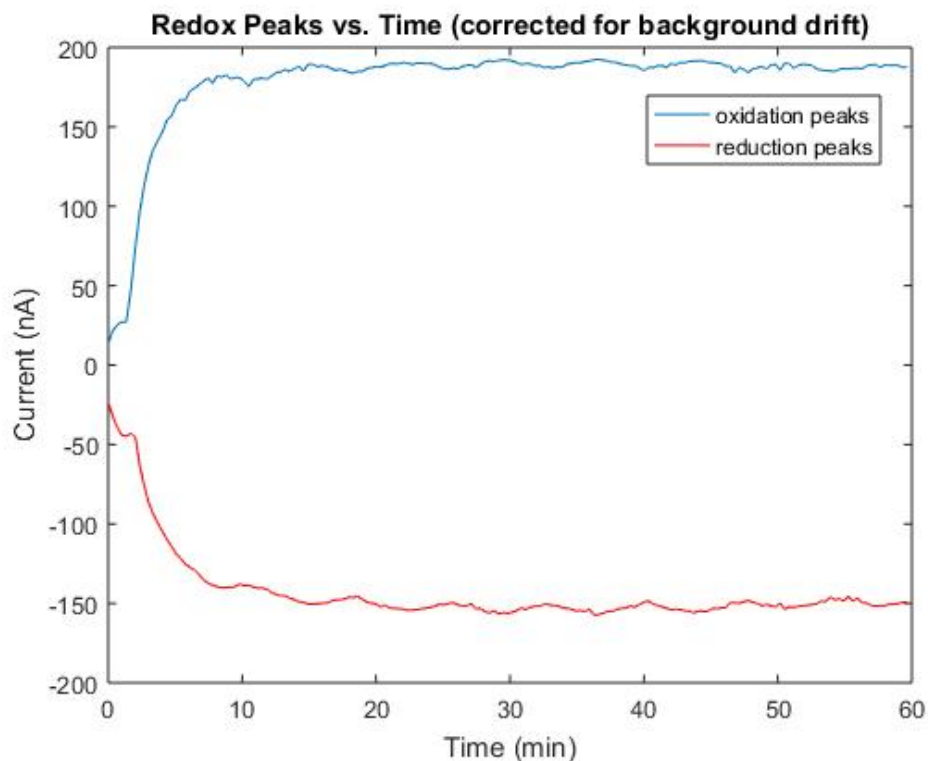

Figure 4.2: Oxidation/reduction current after background drift correction.

Using the corrected plot, it is possible to determine the time required for the dopamine concentration to rise from 10% to 90% of the step change, which is an important indicator for Taylor dispersion. The approximate rise time based on the oxidation and reduction curves is 4.7 minutes and 6.7 minutes, respectively. The rise time takes several minutes, signifying severe Taylor dispersion and very poor temporal resolution. We expected poor temporal resolution from this initial experiment since (1) long flow paths cause a large degree of Taylor dispersion, and the fluid input and analysis chip are separated by several centimeters of tubing, and (2) the PDMS channel cross section (2 mm by 2 mm) is magnitudes larger than that in the tubing (inner diameter of 320 µm), causing a large amount of undesired mixing at this junction that leads to even lower temporal resolution.

Eventually, since the goal is to observe dispersion effects arising from the

packaged probe, we need to conduct experiments with a silicon nanofluidic probe at the input. Hence, it is essential to minimize dispersion in all other parts of the setup. We can significantly reduce the inherent dispersion effects of the flow system by shortening the fluidic path between the input and the analysis chip and by reducing the dimensions of the PDMS channels. The shortest possible fluidic path would completely bypass the plastic tubing by directly connecting the capillaries from the packaged probe to the analysis chip, which is an option that will explored in future designs. Miniaturizing the PDMS channels, however, may be more challenging. We have demonstrated fluid flow through PDMS channels with thicknesses as small as 10 µm, in which Taylor dispersion could be greatly mitigated. However, at this scale it is very difficult to embed FSCV electrodes in the channel and maintain their functionality since there is only 10 µm tolerance when inserting electrodes from the vertical direction. This technical challenge may be more manageable if the PDMS channel thickness is slightly increased (to 25-50 µm, for example) or if the FSCV electrodes are inserted horizontally rather than vertically.

CHAPTER 5

CONCLUSION

We have developed a simple, well-controlled process for fabricating bulk silicon nanofluidic channels and are able to successfully integrate them onto ultrathin silicon probes with less than 20 µm thickness. Moreover, we have built experimental test benches to quantify the fluidic and chemical transport properties of each channel and probe design, which will ultimately determine their suitability for in vivo use. Using the fluidic test bench, we were not able to establish fluid flow through the fully integrated silicon probes, even though simulations predict that flow through the silicon channels is achievable with moderate applied pressures. The next iteration of channel structures, which have lower hydrodynamic resistance and can be operated without probe integration, should reveal whether this issue is caused by channel resistance or flow obstruction. Our chemical transport test bench is based on a novel approach for on-line chemical analysis using FSCV to measure Taylor dispersion effects. Nevertheless, multiple revisions including miniaturization of the analysis chip should be implemented before we can reliably measure Taylor dispersion effects within our silicon probes. Overall, in this work, we have established specific aims for a silicon nanofluidic platform, built crucial components of this platform, and developed the means to evaluate its potential for neurosensing applications.

REFERENCES

[1] B. Bozorgzadeh, D. R. Schuweiler, M. J. Bobak, P. A. Garris, and P. Mohseni, "Neurochemostat: a neural interface soc with integrated chemometrics for closed-loop regulation of brain dopamine," *IEEE Trans Biomed Circuits Syst*, vol. 10, no. 3, pp. 654-667, Jun. 2016.

[2] N. Cellar, S. T. Burns, J.-C. Meiners, H. Chen, and R. T. Kennedy, "Microfluidic chip for low-flow push-pull perfusion sampling in vivo with on-line analysis of amino acids," *Analytical Chemistry*, vol. 77, no. 21, pp. 7067-7073, 2005.

[3] D. E. Cepeda, L. Hains, D. Li, J. Bull, S. I. Lentz, and R. T. Kennedy, "Experimental evaluation and computational modeling of tissue damage from low-flow push-pull perfusion sampling in vivo," *J Neurosci Methods*, vol. 242, pp. 97-105, Mar. 2015.

[4] C. Chen, B. T. Rasley, B. P. E. Warlick, T. K. Green, K. E. Swearingen, and K. L. Drew, "Microdialysis and advances for sampling synaptic and extrasynaptic pools," in *Microdialysis Techniques in Neuroscience*, 2013, pp. 63-88.

[5] K. C. Cheung, K. Djupsund, Y. Dan, and L. P. Lee, "Implantable multichannel electrode array based on SOI technology," *Journal of Microelectromechanical Systems*, vol. 12, no. 2, pp. 179-184, 2003.

[6] V. H. Cifuentes Castro et al., "An update of the classical and novel methods used for measuring fast neurotransmitters during normal and brain altered function," *Current Neuropharmacology*, vol. 12, no. 6, pp. 490-508, 2014.

[7] M. Ganesana, S. T. Lee, Y. Wang, and B. J. Venton, "Analytical techniques in neuroscience: recent advances in imaging, separation, and electrochemical methods," *Analytical Chemistry*, vol. 89, no. 1, pp. 314-341, Jan. 2017.

[8] A. L. Hogerton and M. T. Bowser, "Monitoring neurochemical release from astrocytes using in vitro microdialysis coupled with high-speed capillary electrophoresis," *Analytical Chemistry*, vol. 85, no. 19, pp. 9070-9077, Oct. 2013.

[9] P. J. Hutchinson et al., "Clinical cerebral microdialysis: a methodological study," *Journal of Neurosurgery*, vol. 93, pp. 37-43, 2000.

[10] T. Ngernsutivorakul, T. S. White, and R. T. Kennedy, "Microfabricated probes for studying brain chemistry: A review," *Chem. Phys. Chem*, vol. 19, no. 10, pp. 1128-1142, May 2018.

[11] G. Petit-Pierre, A. Bertsch, and P. Renaud, "Neural probe combining microelectrodes and a droplet-based microdialysis collection system for high temporal resolution sampling," *Lab Chip*, vol. 16, no. 5, pp. 917-924, Mar. 2016.

[12] S. A. N. Gowers et al., "High temporal resolution delayed analysis of clinical microdialysate streams," *Analyst*, vol. 143, no. 3, pp. 715-724, Jan. 2018.

[13] W. H. Lee et al., "Microfabrication and in vivo performance of a microdialysis probe with embedded membrane," *Analytical Chemistry*, vol. 88, no. 2, pp. 1230-1237, Jan. 2016.

[14] W. H. Lee, T. R. Slaney, R. W. Hower, and R. T. Kennedy, "Microfabricated sampling probes for in vivo monitoring of neurotransmitters," *Analytical Chemistry*, vol. 85, no. 8, pp. 3828-3831, Apr. 2013.

[15] G. Petit-Pierre et al., "In vivo neurochemical measurements in cerebral tissues using a droplet-based monitoring system," *Nat Commun*, vol. 8, no. 1, p. 1239, Nov. 2017.

[16] A. G. Zestos and R. T. Kennedy, "Microdialysis coupled with LC-MS/MS for in vivo neurochemical monitoring," *AAPS J*, vol. 19, no. 5, pp. 1284-1293, Sept. 2017.

[17] M. W. Lada, T. W. Vickroy, and R. T. Kennedy, "High temporal resolution monitoring of glutamate and aspartate in vivo using microdialysis on-line with capillary electrophoresis with laser-induced fluorescence detection," *Analytical Chemistry*, vol. 69, pp. 4560-4565, 1997.

[18] T. S. Shippenberg and A. C. Thompson, "Overview of microdialysis," in *Current Protocols in Neuroscience*: John Wiley and Sons, Inc., 1997.

[19] T. R. Slaney et al., "Push-pull perfusion sampling with segmented flow for high temporal and spatial resolution in vivo chemical monitoring," *Analytical Chemistry*, vol. 83, no. 13, pp. 5207-5213, Jul. 2011.

[20] M. Wang, G. T. Roman, M. L. Perry, and R. T. Kennedy, "Microfluidic chip for high efficiency electrophoretic analysis of segmented flow from a microdialysis probe and in vivo chemical monitoring," *Analytical Chemistry*, vol. 81, pp. 9072-9078, 2009.

[21] M. Wang, G. T. Roman, K. Schultz, C. Jennings, and R. T. Kennedy, "Improved temporal resolution for in vivo microdialysis by using segmented flow," *Analytical Chemistry*, vol. 80, no. 14, pp. 5607-5615, 2008.

[22] M. Wang, T. Slaney, O. Mabrouk, and R. T. Kennedy, "Collection of nanoliter microdialysate fractions in plugs for off-line in vivo chemical monitoring with up to 2 s temporal resolution," *J Neurosci Methods*, vol. 190, no. 1, pp. 39-48, Jun. 2010.

[23] A. A. Kim et al., "SU-8 free-standing microfluidic probes," *Biomicrofluidics*, vol. 11, 2017.

[24] G. Taylor, "Dispersion of soluble matter in solvent flowing slowly through a tube," in *Proceedings of the Royal Society A: Mathematical, Physical and Engineering Sciences*, vol. 219, no. 1137, pp. 186-203, 1953.